Research Article

Nano Research
2020, 13(8): 2044–2055

ISSN 1998-0124 CN 11-5974/O4
https://doi.org/10.1007/s12274-020-2806-9

Facile synthesis of Au embedded CuO_x–CeO_2 core/shell nanospheres as highly reactive and sinter-resistant catalysts for catalytic hydrogenation of p-nitrophenol

Ke Wu[1,§], Xin-Yu Wang[1,§], Ling-Ling Guo[2], Yue-Jiao Xu[1], Liang Zhou[1], Ze-Yu Lyu[1], Kang-Yu Liu[1], Rui Si[2], Ya-Wen Zhang[1], Ling-Dong Sun[1] (✉), and Chun-Hua Yan[1,3] (✉)

[1] *Beijing National Laboratory for Molecular Sciences, State Key Laboratory of Rare Earth Materials Chemistry and Applications, PKU-HKU Joint Laboratory in Rare Earth Materials and Bioinorganic Chemistry, and College of Chemistry and Molecular Engineering, Peking University, Beijing 100871, China*

[2] *Shanghai Synchrotron Radiation Facility, Shanghai Institute of Applied Physics, Chinese Academy of Sciences, Shanghai 201204, China*

[3] *College of Chemistry and Chemical Engineering, Lanzhou University, Lanzhou 730000, China*

[§] *Ke Wu and Xin-Yu Wang contributed equally to this work.*

Received: 19 February 2020 / **Revised:** 24 March 2020 / **Accepted:** 10 April 2020

ABSTRACT

Exploring cost-effective catalysts with high catalytic performance and long-term stability has always been a general concern for environment protection and energy conversion. Here, Au nanoparticles (NPs) embedded CuO_x–CeO_2 core/shell nanospheres (Au@CuO_x–CeO_2 CSNs) have been successfully prepared through a versatile one-pot method at ambient conditions. The spontaneous auto-redox reaction between $HAuCl_4$ and $Ce(OH)_3$ in aqueous solution triggered the self-assembly growth of micro-/nanostructural Au@CuO_x–CeO_2 CSNs. Meanwhile, the CuO_x clusters in Au@CuO_x–CeO_2 CSNs are capable of improving the anti-sintering ability of Au NPs and providing synergistic catalysis benefits. As a result, the confined Au NPs exhibited extraordinary thermal stability even at a harsh thermal condition up to 700 °C. In addition, before and after the severe calcination process, Au@CuO_x–CeO_2 CSNs can exhibit enhanced catalytic activity and excellent recyclability towards the hydrogenation of p-nitrophenol compared to previously reported nanocatalysts. The synergistic catalysis path between Au/CuO_x/CeO_2 triphasic interfaces was revealed by density functional theory (DFT) calculations. The CuO_x clusters around the embedded Au NPs can provide moderate adsorption strength of p-nitrophenol, while the adjacent CeO_2-supported Au NPs can facilitate the hydrogen dissociation to form H* species, which contributes to achieve the efficient reduction of p-nitrophenol. This study opens up new possibilities for developing high-efficient and sintering-resistant micro-/nanostructural nanocatalysts by exploiting multiphasic systems.

KEYWORDS

core/shell nanostructure, sinter-resistant catalysts, triphasic interfaces catalysis, p-nitrophenol reduction

1 Introduction

Nitrophenols, as one of the toxic organic contaminants substantially produced from agricultural and industrial manufacturing processes, are harmful to human blood cells and the central neural system [1]. Hence, it is in urgent need to transform the nitroaromatic compounds to more benign products [2]. Nowadays, various methods have been utilized for the removal of p-nitrophenols from environment, such as photocatalytic degradation, and electrochemical treatment, etc. However, the tedious treatment steps and sky-scraping cost greatly restrict the practical applications of these methods. By contrast, the facile catalytic reduction of p-nitrophenols into useful p-aminophenol catalyzed by noble metal nanocatalysts has become a promising alternative [3]. Recently, Au-related nanomaterials have been reported to be efficient for the catalytic hydrogenation of p-nitrophenol. However, owing to the high surface energy, pristine Au NPs-based catalysts are usually unstable and susceptible to severe aggregation during catalytic processes [4]. The undesired sintering of Au NPs into larger particles can lead to rapid degradation of the catalytic activity, which seriously hinder their applications in industrial catalysis [5]. To solve this problem, anchoring Au NPs into a suitable support material was proposed to diminish the deleterious agglomeration and improve the long-term stability of nanocatalysts. The enhanced chemical bonding at the metal-support interface can be responsible for preventing the migration of metal atoms on the support [6]. Therefore, the stronger metal-support interaction should benefit to retarding the sintering process of Au NPs. Furthermore, the multifunctionality that derived from metal-support interface has been corroborated for providing specific pathways for hydrogenation of p-nitrophenol, and thus contributing to the enhanced catalytic performance [7].

CeO_2 has been widely recognized as active supports for Au NPs, which particularly facilitates the reactivity of supported Au atoms located at the Au–CeO_2 interface perimeter [8]. Moreover, it has been demonstrated that smaller Au NPs can

Address correspondence to Ling-Dong Sun, sun@pku.edu.cn; Chun-Hua Yan, yan@pku.edu.cn

be maintained and the corresponding sintering process will slow down on the CeO_2 substrate [9]. Besides, with the structural integrity of CeO_2, the oxidation state of Ce element in CeO_2 can facilely switch between Ce(III) and Ce(IV) [10]. The resulting Ce(III) can play the role of Lewis base to activate the substrate adsorption and thus improves the catalytic activity [11]. As a consequence, intensive attention has been paid to modify the interfacial effects between Au NPs and CeO_2 support, and further develop well-tuned nanostructures to realize the superior performance and durability for catalytic applications [12–15]. Among various Au/CeO_2 composites, core/shell structural composites encapsulating the catalytically active Au NPs in porous CeO_2 shells with numerous void spaces are decent candidates for highly-efficient anti-sintering catalysis on accounts of large surface areas, low density, and especially designable hollow interspaces [16–18].

In addition to constructing ceria shells as protective layers to prohibit the embedded Au NPs from sintering, dual-oxide support can also be utilized to enhance the resistance to sintering through providing extra energy barriers [19]. The energy barrier for migration of Au NPs across the dual-oxide support to merge into larger particles is much greater than that across the common single-oxide support [20]. As a result, the sintering of Au NPs through surface diffusion route can be effectively suppressed. CuO_x species have been verified beneficial to the anchoring the Au NPs on the support, and stabilizing the embedded Au NPs within limited size dimension for increased resistance to sintering [21]. Meanwhile, the catalytic performance of ceria-encapsulated Au NPs could also be enhanced via the addition of CuO_x clusters. For example, recent progresses have unraveled the improved catalytic activity of CuO for the hydrogenation of p-nitrophenol [22, 23]. It is also noteworthy that integration of dual-metal oxide phases into closely-coupled Au NPs can result in synergistic catalysis effect, which has been successfully applied to promote the catalytic performance [17, 24]. More recently, numerous successful attempts have been realized on the basis of the interfacial auto-catalytic redox reactions for preparing ceria-encapsulated noble metal or transition metal oxide nanocatalysts with core/shell nanostructures [25]. For instance, our group has developed a novel method for preparing Pt-embedded CuO_x–CeO_2 multicore-shell nanostructures at room temperature [26]. However, an effective strategy for the integration of Au NPs and CuO_x–CeO_2 support with core/shell structure has not been realized yet.

Herein, we developed a facile and green synthesis route for preparing Au NPs embedded CuO_x–CeO_2 core/shell nanospheres (Au@CuO_x–CeO_2 CSNs) at ambient conditions. Interestingly, the close proximity between CuO_x clusters and adjacent Au NPs can increase the resistance to sintering of embedded Au NPs at elevated temperature. Therefore, after the high-temperature treatment at 700 °C, Au@CuO_x–CeO_2 CSNs can still exhibit superior catalytic activity and long-term durability for p-nitrophenol reduction reaction when compared with Au@CeO_2 CSNs and CuO_x–CeO_2 counterparts. Importantly, further investigation from DFT calculations revealed that CuO_x clusters around the embedded Au NPs benefiting to the optimal adsorption strength of p-nitrophenol. In addition, Au NPs supported on CeO_2 has evidenced to be responsible for the cleavage of H–H bonds to produce H* species, and thus induces the synergistic catalysis effect in Au/CuO_x/CeO_2 interface. Consequently, the catalytic performance of Au@CuO_x–CeO_2 CSNs for p-nitrophenol hydrogenation can be notably enhanced.

2 Results and discussion

2.1 Synthesis and characterization of Au@CuO_x–CeO_2 CSNs

The synthetic illustration for Au@CuO_x–CeO_2 CSNs is described in Fig. 1. Firstly, the auto-redox reaction occurred between the interface of reductive $Ce(OH)_3$ and oxidative Au(III) ions, which produced small-sized CeO_2 nanospheres and Au NPs, respectively [27]. Meanwhile, the as-added Cu(II) ions will be converted to $Cu(OH)_x$ in the existing alkaline solution, and further spontaneously adhered to the surface of as-formed CeO_2 nanospheres to produce $Cu(OH)_x$/CeO_2 hybrids driven by the electrostatic interaction, which can be described as the typical deposition-precipitation (DP) process [28]. After that, due to the van der Waals attraction, Au NPs and surrounding $Cu(OH)_x$/CeO_2 nanospheres were apt to grow into micro-/nanostructural aggregates with spherical morphology. Moreover, when the electrostatic-repulsion interaction between the nanospheres in aggregates and newly-reached nanospheres achieved a balance of their attractive interaction, the self-assemble process will be terminated [29]. Finally, after the air-calcinated treatment process, the Au@CuO_x–CeO_2 CSNs can be obtained. Importantly, when the precursors of noble metal salts changing from $HAuCl_4$ to K_2PtCl_4, core/shell structural Pt@CuO_x–CeO_2 nanocomposites were also successfully prepared (Fig. S1 in the Electronic Supplementary Material (ESM)), which demonstrated the versatility of the present synthesis strategy. In addition, without $CuCl_2$ precursors during the synthesis of Au@CuO_x–CeO_2 CSNs, only ununiformly-dispersed Au@CeO_2 CSNs nanohybrids can be obtained due to the increased auto-redox reaction rate (Fig. S2 in the ESM). Furthermore, the CuO_x–CeO_2 reference catalysts were also prepared via the DP method for the comparison of catalytic performance (Fig. S3 in the ESM).

The detailed morphology and composition of Au@CuO_x–CeO_2 CSNs were further investigated by transmission electron microscopy (TEM) characterization. As shown in Fig. 2(a), sphere-like particles with a narrow size distribution of ca. 52.9 ± 5.1 nm can be observed in large scale from TEM image, which is basically in line with the corresponding hydrodynamic diameter of 63.7 ± 1.2 nm (Fig. S4 in the ESM). The selected area electron diffraction (SAED) image in Fig. 2(b) showed typical circular diffraction rings, directly confirming the polycrystalline structure of Au@CuO_x–CeO_2 CSNs, and can be principally indexed to ceria with cubic-fluorite structure [4]. Moreover, an obscure diffraction ring that corresponds to characteristic diffraction from (111) facet of Au can be carefully distinguished, suggesting the occurrence of auto-redox reaction can ensure the Au(III) precursors completely reduced [30].

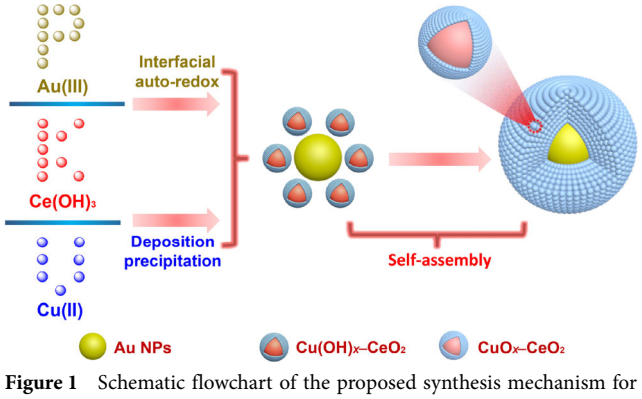

Figure 1 Schematic flowchart of the proposed synthesis mechanism for Au@CuO_x–CeO_2 CSNs.

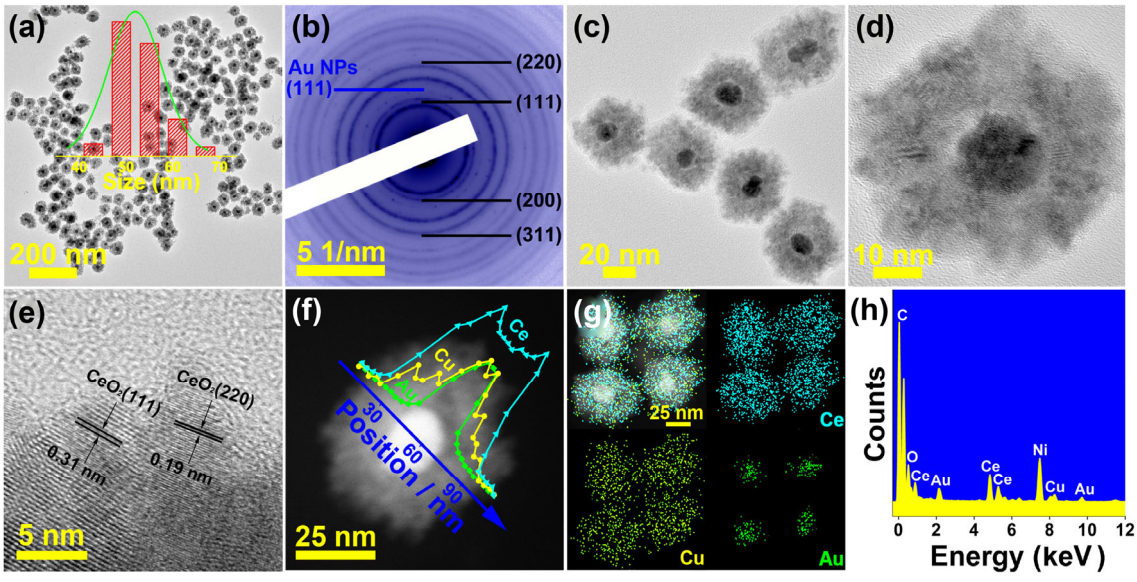

Figure 2 TEM characterizations of Au@CuO_x–CeO_2 CSNs. (a) Large-scale TEM images, the illustration in (a) is the resulting size distribution diagram. (b) SAED pattern. (c) and (d) Magnified TEM images. (e) HRTEM image. (f) HAADF-STEM, the inset in (f) showed the corresponding EDS linear scanning profile of one Au@CuO_x–CeO_2 CSNs particle. (g) elemental mapping images. (h) EDS analysis.

Additionally, the magnified TEM images in Figs. 2(c) and 2(d) show strong evidence for the core/shell micro-/nanostructure of Au@CuO_x–CeO_2 CSNs, where the interface between entrapped Au NPs and densely-interconnected CuO_x–CeO_2 nanospheres can be clearly observed.

Figure 2(e) shows the resulting high-resolution TEM (HRTEM) image. Two sets of lattices fringe with interplanar spacing of 0.19 and 0.31 nm can be observed, which can be indexed to the (220) and (111) facets of CeO_2, respectively [31]. In addition, as shown in Fig. 2(f), the high-angle annular dark-field scanning transmission electron microscopy (HAADF-STEM) image further verified the core/shell structural Au@CuO_x–CeO_2 CSNs through image contrast, in which the inner bright part should be ascribed to the embedded Au NPs with higher atomic numbers [32]. The elements distribution of Au@CuO_x–CeO_2 CSNs composites were studied via the energy dispersive X-ray spectroscopy (EDS) linear-scanning and STEM-mapping technique. For a single particle, the corresponding EDS line scanning in Fig. 2(f) and mapping profiles in Fig. 2(g) show that Au NPs were mainly located in the core region and integrally wrapped by self-supported CuO_x–CeO_2 nanospheres, indicating the core/shell structure of Au@CuO_x–CeO_2 CSNs. The EDS data in Fig. 2(h) revealed the [Au]/[Cu] ratio of Au@CuO_x–CeO_2 CSNs is ca. 1/1, which matched well with the result (52:48) from inductively coupled plasma optical emission spectroscopy (ICP-OES) (Table S1 in the ESM). Notably, the measured Cu content were lower than its feed ratio, which should be due to the short time of the rapid auto-redox reaction and successive self-assemble process, thus reducing the amount of $Cu(OH)_x$ species on ceria nanospheres.

2.2 Catalytic performance of Au@CuO_x–CeO_2 CSNs for p-nitrophenol reduction

In order to quantitatively evaluate the catalytic performance of Au@CuO_x–CeO_2 CSNs, the catalytic hydrogenation of p-nitrophenol to p-aminophenol is chosen as a model reaction with an excess of freshly-prepared $NaBH_4$ at ambient temperature. This reaction has also been employed to be a facile and eco-friendly method for producing p-nitrophenol in industries [33]. As shown in Fig. S5 in the ESM, without the addition of $NaBH_4$, p-nitrophenol solution showed a broad absorption peak at about 320 nm. Upon the introduction of $NaBH_4$, a spectral red-shift to 400 nm can be observed (Fig. S5 in the ESM), which was due to the formation of p-nitrophenolate ions in alkaline medium [34]. Furthermore, in the absence of reductive agents (Fig. S6(a) in the ESM), the adsorption peak at 320 nm hardly changed for as long as 60 min, thus excluding the physical adsorption effect of p-nitrophenol by Au@CuO_x–CeO_2 CSNs. Similarly, as shown in Fig. S6(b) in the ESM, without adding the Au@CuO_x–CeO_2 CSNs, the non-catalytic reduction reaction hardly proceeded in the forward direction. Nevertheless, as the Au@CuO_x–CeO_2 CSNs was rapidly injected into the reaction cuvette containing p-nitrophenol and $NaBH_4$ solution, the hydrogenation reaction was instantly triggered, and the primary yellow solution become colorless quickly. At the same time, the characteristic absorption peak intensity at 400 nm in Fig. 3(a) decreased sharply over time. Concomitantly, at around 300 nm, a new and weak absorption peak can be observed, which can be ascribed to the products of p-aminophenol. Interestingly, the complete conversion of p-nitrophenol to p-aminophenol over Au@CuO_x–CeO_2 CSNs can be realized within 5 min, which was much faster than that of CuO_x–CeO_2 (10 min, Fig. 3(b)) and Au@CeO_2 CSNs counterparts (15 min, Fig. 3(c)), thus proving the dramatic increase in catalytic activity of Au@CuO_x–CeO_2 CSNs. During the catalytic process, the concentration of $NaBH_4$ was considered to be largely more than that of p-nitrophenol, thus the consumption of $NaBH_4$ can be almost negligible. Hence, the concentration of $NaBH_4$ can be reasonably regarded as an unchanged constant. By this means, the rate of the hydrogenation reaction could only be dependent on the concentration of p-nitrophenol, and seen as a typical pseudo-first-order reaction [35]. As a result, the apparent rate constant (k) can be calculated from the following equation:

$$\ln(C_t/C_0) = -kt$$

Here, the value of C_t/C_0 represents the ratio of p-nitrophenol concentration at time t to its initial concentration (0 min), and was acquired from their relative absorbance intensity at 400 nm (A_t/A_0) [36]. As shown in Fig. 3(d), all the measured samples showed linear correlation between $\ln(C_t/C_0)$ and reaction time (t). The rate constant (k) for Au@CuO_x–CeO_2 CSNs shown in

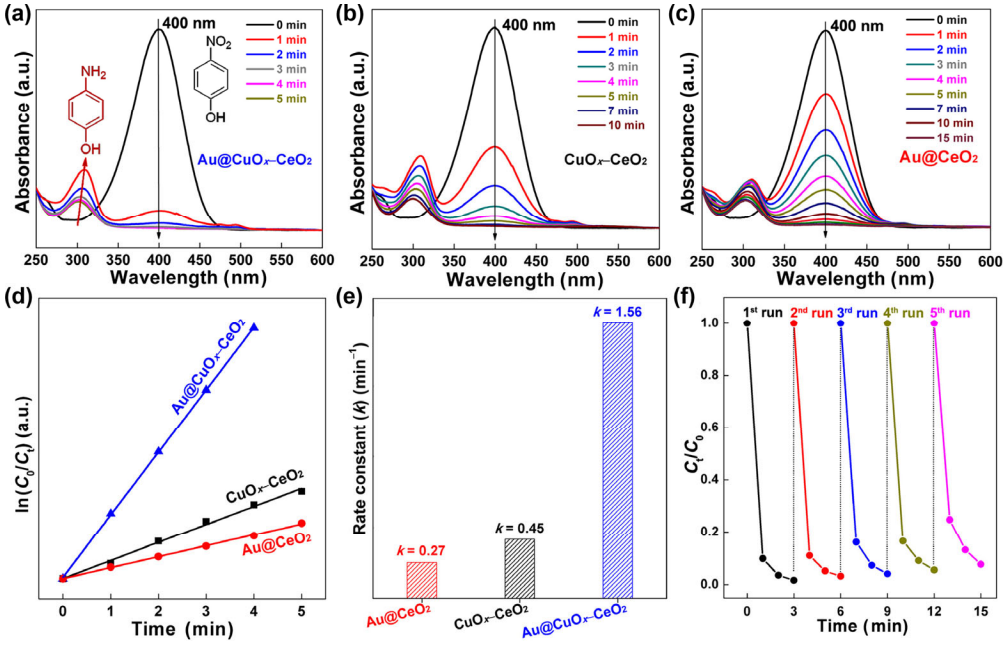

Figure 3 Time-dependent UV–vis absorbance spectra during the catalytic hydrogenation of p-nitrophenol by $NaBH_4$ over Au@CuO_x–CeO_2 CSNs (a), the reference catalysts of CuO_x–CeO_2 (b), and Au@CeO_2 CSNs counterpart (c). The resulting plots of $\ln(C_0/C_t)$ versus the reaction time (d) and the corresponding histogram of rate constants for as-measured catalysts (e). The reusability of Au@CuO_x–CeO_2 CSNs for the reduction of p-nitrophenol in five successive cycles (f).

Fig. 3(e) were calculated to be 1.56 min^{-1}, which is 3.5 and 5.8 times higher than that of CuO_x–CeO_2 (0.45 min^{-1}) and Au@CeO_2 (0.27 min^{-1}), respectively.

Moreover, the recyclability test was carried out to study the durability of Au@CuO_x–CeO_2 CSNs for the catalytic reduction of p-nitrophenol. As shown in Fig. 3(f), after five successive cycles of hydrogenation reactions, the catalytic activity of Au@CuO_x–CeO_2 CSNs did not exhibit significant decrease as compared to the first cycle. Besides, the conversion ratio of p-nitrophenol can still be maintained up to ca. 92% within 3 min, and the primary core/shell structural morphology of the Au@CuO_x–CeO_2 CSNs are also well-preserved (Fig. S7 in the ESM). The above results highlight an excellent reusability of Au@CuO_x–CeO_2 CSNs for the catalytic reduction of p-nitrophenol. Meanwhile, Fig. 4 and Table S2 in the ESM summarized the comparison of catalytic activity between Au@CuO_x–CeO_2 CSNs and recently reported Au NPs-based nanocatalysts for the direct hydrogenation of p-nitrophenol [1, 8, 20, 37–42]. The comparison further confirmed the superior catalytic performance of as-prepared Au@CuO_x–CeO_2 CSNs.

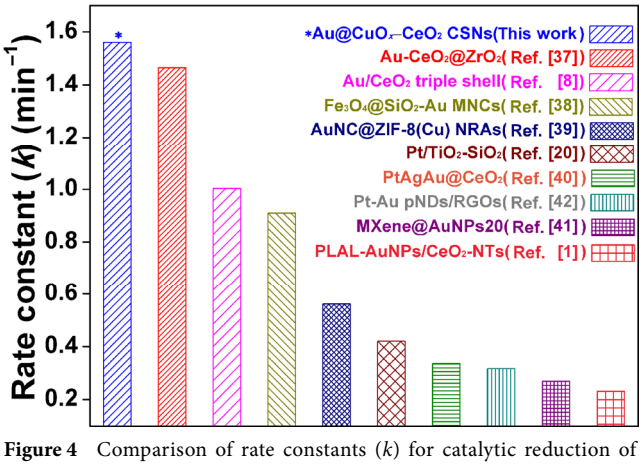

Figure 4 Comparison of rate constants (k) for catalytic reduction of p-nitrophenol over Au@CuO_x–CeO_2 CSNs with previously-reported nanocatalysts.

2.3 Sinter-resistant property of Au@CuO_x–CeO_2 CSNs

We examined the thermal stability of the Au@CuO_x–CeO_2 CSNs by calcinating the as-prepared nanocatalysts at high temperatures up to 700 °C under air atmosphere for 2 h. As shown in Fig. 5(a), the core/shell structure of Au@CuO_x–CeO_2_700 CSNs can still be well preserved. Moreover, it is obvious that the coarsening behavior of the embedded Au NPs was greatly suppressed, which should be due to the efficient encapsulation of surrounding CuO_x–CeO_2 self-assembled nanospheres [43]. From the TEM image in Fig. 5(b), (200)-terminated facets of ceria can be clearly recognized, which should be ascribed to the reconstruction of CeO_2(110) facets when calcinated in high temperature [44]. Moreover, the resulting EDS linear scanning profile (Fig. 5(c)) and EDS mapping pattern (Fig. 5(d)) further illustrated that CuO_x clusters still spread over the Au@CuO_x–CeO_2_700 CSNs and tend to concentrate around the embedded Au NPs after the high-temperature calcination. Analogously, as shown in Fig. S8 in the ESM, the CuO_x clusters that uniformly-distributed on the reference catalysts of CuO_x–CeO_2_700 also maintain the homogeneous dispersion as before. On the contrary, without CuO_x clusters, Au@CeO_2_700 CSNs reference catalysts underwent severe agglomeration as illustrated in Fig. S9 in the ESM. The X-ray diffraction (XRD) patterns of Au@CuO_x–CeO_2 CSNs before and after calcination at 700 °C were shown in Fig. 5(e). The resulting diffraction peaks can be ascribed to two distinct phases, which consist of fluorite-structured CeO_2 and face-centered cubic crystal structure of Au [4]. Based on the Scherrer equation, the crystallite size (d_{XRD}) of the embedded Au NPs calculated from the reflection of Au (111) at about 38° is about 7.4 nm. Meaningfully, due to the high dispersion of CuO_x clusters, typical diffractions concerning CuO_x species cannot be detected, which resembles the XRD patterns of CuO_x–CeO_2 and CuO_x–CeO_2_700 in Fig. S10 in the ESM [45, 46]. After the high-temperature calcination, the diffraction peak of CeO_2 in Au@CuO_x–CeO_2_700 CSNs become slightly sharpened, which should be attributed to the enhanced crystallization degree at high temperature. Similarly, the diffractions of Au NPs in

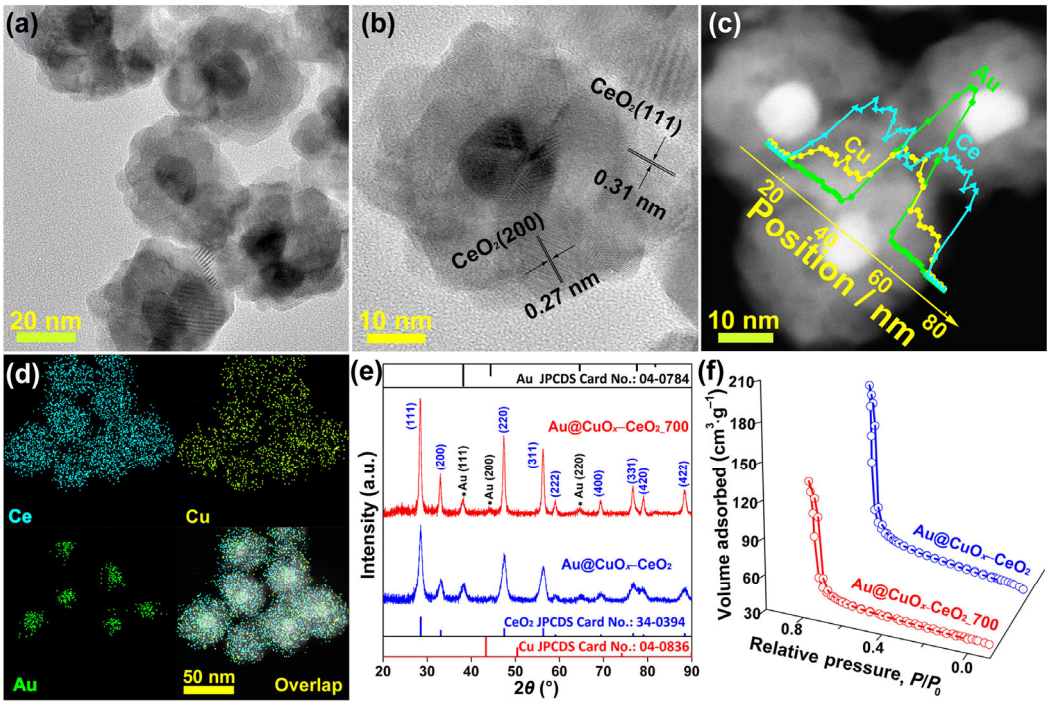

Figure 5 (a) and (b) TEM images of Au@CuO_x–CeO_2_700 CSNs with various magnifications; (c) HAADF-STEM image (insert: EDS line-scan profile of one Au@CuO_x–CeO_2_700 CSNs particle). (d) EDS mapping images. Typical XRD patterns (e) and nitrogen adsorption and desorption isotherm (f) of Au@CuO_x–CeO_2 CSNs and Au@CuO_x–CeO_2_700 CSNs.

Au@CuO_x–CeO_2_700 CSNs did not experience apparent change, and the resulting d_{XRD} value was measured to be 11.7 nm according to Scherrer equation analysis [47]. In contrast, the d_{XRD} value of embedded Au NPs in Au@CeO_2 CSNs before and after the high-temperature process was quantified to be 9.7 nm and 15.7 nm, respectively (Fig. S11 in the ESM). These results verified the superior structural and thermal stability of Au@CuO_x–CeO_2 CSNs, and the remarkably increased crystallite size of Au@CeO_2_700 CSNs directly demonstrate the efficient protection of highly-dispersed CuO_x clusters against the coarsening behaviour of the entrapped Au NPs [21, 48].

In addition, the porous structure and surface area of Au@CuO_x–CeO_2 CSNs and Au@CuO_x–CeO_2_700 CSNs were characterized by N_2 adsorption-desorption experiments. As shown in Fig. 5(f), the obtained N_2 adsorption-desorption isotherms of Au@CuO_x–CeO_2 CSNs increase steeply at a higher relative pressure, corresponding well to the type IV isotherm in accordance with the classification from IUPAC [49]. Moreover, the typical H3 hysteresis loop of Au@CuO_x–CeO_2 CSNs confirmed the feature of mesoporous materials. Similarly, the resulting isotherms of Au@CuO_x–CeO_2_700 CSNs resembled that of Au@CuO_x–CeO_2 CSNs with decreased adsorbed volume. The Brunauer–Emmett–Teller (BET) surface area of Au@CuO_x–CeO_2 CSNs and Au@CuO_x–CeO_2_700 CSNs were measured to be 54.76 and 22.11 $m^2 \cdot g^{-1}$, respectively. The decline of BET surface area caused by high-temperature calcination was similar to those of the reference catalysts of Au@CeO_2_700 CSNs and CuO_x–CeO_2_700 (Fig. S12 in the ESM). The corresponding pore size distribution of Au@CuO_x–CeO_2 CSNs was calculated according to the analysis of desorption branch by the Barrett-Joyner-Halenda (BJH) method. As shown in Fig. S13 in the ESM, a bimodal pore size distribution was observed for Au@CuO_x–CeO_2 CSNs at around the range of 2–4 nm and 20–40 nm, respectively. The former pores were likely caused by the interparticle space between self-assembled CuO_x–CeO_2 nanospheres [50]. Besides, the larger pores could be ascribed to the interior cavities between the embedded Au NPs and surrounding CuO_x–CeO_2 nanospheres. After the high-temperature calcination, the 2–4 nm-sized pores of Au@CuO_x–CeO_2_700 CSNs disappeared, but the pores larger than 20 nm can still be preserved. Apparently, the high BET surface area and the mesoporous characteristic of Au@CuO_x–CeO_2 CSNs that derived from the loose self-assembled core/shell structures can facilitate the adsorption capability of nitro-compounds and thus enhance the catalytic performance. Despite of the sacrifice of 2–4 nm-sized pores of Au@CuO_x–CeO_2_700 CSNs after the calcination, the existing larger pores of 20–40 nm can still meet the demand for the easy transport of reactant molecules, and should be beneficial for the improvement of catalytic reactivity [51].

Element-selective X-ray absorption fine structure (XAFS) technique, including X-ray absorption near-edge structure (XANES) and the extended X-ray absorption fine structure (EXAFS) were further employed to evaluate the change of chemical states as well as the structural differences of Au@CuO_x–CeO_2 CSNs during the high-temperature treatment. As shown in Fig. 6(a), the adsorption-edge energy and white-line peak height of the normalized Cu-K edge XANES spectra for Au@CuO_x–CeO_2 CSNs were higher than those of Cu foil (metallic Cu). Moreover, the XANES spectral features of both Au@CuO_x–CeO_2 CSNs and Au@CuO_x–CeO_2_700 CSNs were similar to the reference CuO sample. As a result, the prevailing valence state of Cu element in Au@CuO_x–CeO_2 CSNs was identified to be Cu(II) before and after the high-temperature calcination process, which apparently confirming the existences of highly-dispersed CuO_x clusters. In addition, the normalized XANES spectra for Au@CuO_x–CeO_2 CSNs at Au-L_3 edge was identical to that of Au foil in Fig. 6(b), proving that the embedded Au NPs should be predominant in a metallic state. Meanwhile, the CO-DIRFTs spectra in Fig. S14 in the ESM further confirmed the prevailing existence of Au(0) species in Au@CuO_x–CeO_2 CSNs [52]. More importantly, the white-line intensity and line shape of Au@CuO_x–CeO_2_700 CSNs almost remained unchanged after the violent calcination treatment.

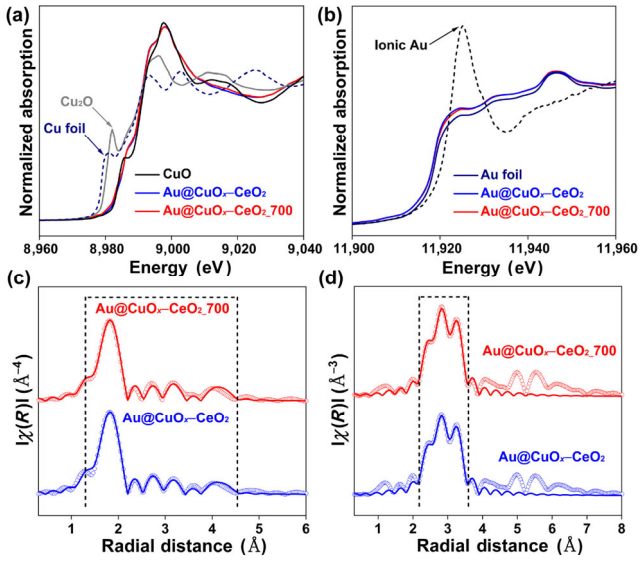

Figure 6 (a) Normalized Cu K-edge and (b) Au L_3-edge XANES profiles of Au@CuO_x–CeO_2 CSNs, Au@CuO_x–CeO_2_700 CSNs and other standard samples. (c) Cu K-edge and (d) Au L_3-edge EXAFS fitting spectra in R space for Au@CuO_x–CeO_2 CSNs and Au@CuO_x–CeO_2_700 CSNs composites (The experimental results were present in open circles, and the fitted data were shown in solid lines).

Hence, the XANES results verified that the dual oxide support of CuO_x–CeO_2 can efficiently protect the metallic Au NPs against overoxidation during high-temperature calcination at 700 °C. The Fourier-transformed (FT) k^3-weighted R-space EXAFS spectra at the Cu K-edge were displayed in Fig. 6(c). The dominant peak attributed to the Cu–O coordination was observed at around 1.93 Å (Table S3 in the ESM) for Au@CuO_x–CeO_2 CSNs before and after the high-temperature calcination, resembling the spectrum of CuO reference. Moreover, the absence of long-range ordered Cu–Cu interaction further corroborated the presence of ultrasmall CuO_x clusters in Au@CuO_x–CeO_2 CSNs. Figure 6(d) showed the corresponding Au L_3-edge FT of k^3-weighted EXAFS spectra (R-space). For Au@CuO_x–CeO_2 CSNs, a pure Au–Au contribution (R = 2.85 ± 0.01 Å, CN = 9.3 ± 0.1) was detected, indicating the embedded Au NPs are metallically dispersed in the matrix. Furthermore, after calcinated at 700 °C, Au@CuO_x–CeO_2_700 CSNs displayed no characteristic peaks corresponding to Au–O contribution compared with the reported ionic Au samples (Table S4 in the ESM) [12]. Consequently, in combination with XANES data, the roles of biphasic CuO_x–CeO_2 support in enhancing the resistance to sintering of encapsulated Au NPs were further confirmed.

X-ray photoelectron spectroscopy (XPS) characterizations were performed to investigate the valence states for the elements in the outer surface of Au@CuO_x–CeO_2 CSNs samples with or without the high-temperature calcination process. Figure 7(a) showed the high-resolution XPS spectra of Ce 3d for Au@CuO_x–CeO_2 CSNs before and after the high-temperature calcination. The resulting XPS peaks of Ce 3d can be mainly deconvoluted to a binary oxidation states of Ce(III) and Ce(IV), which were described as red lines and blue lines, respectively. Therefore, the quasi-quantitative surface Ce(III) concentration over Au@CuO_x–CeO_2 CSNs was calculated to be ca. 23.0%, which is higher than that of Au@CuO_x–CeO_2_700 CSNs counterparts (14.9%) [53]. The slightly decreased content of surface Ce(III) for Au@CuO_x–CeO_2_700 CSNs should be ascribed to the elimination of oxygen vacancies when calcinated at high temperature, leading to the increased oxidation state. The O 1s XPS spectra shown in Fig. 7(b) were deconvolved to

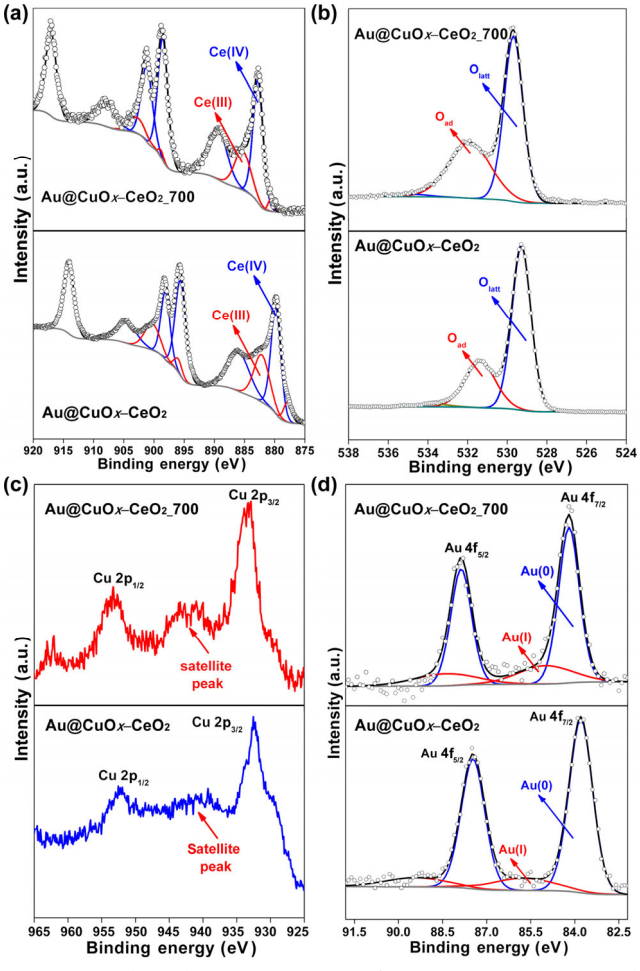

Figure 7 High-resolution XPS spectra of Au@CuO_x–CeO_2 CSNs and Au@CuO_x–CeO_2_700 CSNs: (a) Ce 3d, (b) O 1s, (c) Cu 2p, and (d) Au 4f.

be three different characteristic sub-peaks. The intense peak at lower binding energy of about 529.3 eV corresponded to the lattice oxygen atoms, while the broad peak appeared at 531.4 eV was attributed to surface oxygen species. Furthermore, the negligible peak at 533.4 eV should be the characteristic of adsorbed water. Generally, the surface oxygen species are considered to be associated with the formation of oxygen vacancies, and thus should be proportional to the amount of Ce(III) [31]. However, the resulting concentration of surface oxygen species for Au@CuO_x–CeO_2_700 CSNs (41.3%) is higher than that of Au@CuO_x–CeO_2 CSNs (30.0%).

This phenomenon can be attributed to the existence of highly-dispersed CuO_x clusters. Thus, after the high-temperature calcination process, the oxidation state of Cu in CuO_x clusters tend to get increased, which is clearly evidenced by the increasing intensity for the shake-up satellite peak of Cu 2p XPS spectra in Fig. 7(c) [28, 53]. Therefore, more surface oxygen species will be introduced to make the charge balance in Au@CuO_x–CeO_2_700 CSNs, which is consistent with the result from O 1s XPS spectra. The anti-sintering effect of Au@CuO_x–CeO_2 CSNs can be directly evaluated by the XPS spectra of Au 4f in Fig. 7(d). Namely, the two sharp peaks at 83.8 and 87.5 eV in Au@CuO_x–CeO_2 CSNs indicate the dominant existence of Au(0) species, while the other two weak peaks at 85.7 and 89.4 eV are assigned to the Au^+ species [1, 54]. Moreover, the relative amount of Au(0) for Au@CuO_x–CeO_2 CSNs and Au@CuO_x–CeO_2_700 CSNs were calculated to be 84.4% and 76.4%, respectively. For Au@CeO_2 CSNs, the calculated Au(0) concentration was 89.0% (Table S1 and Fig. S15 in the ESM). The lower ratio of Au(0) in Au@CuO_x–CeO_2

CSNs further disclosed it should be a well-defined core/shell structure, with the embedded Au NPs completely encapsulated by the nearby CuO_x–CeO_2 nanospheres. After the high-temperature calcination, only 70.5% Au(0) can be preserved for Au@CeO_2_700 CSNs, indicating the frangible oxidation of Au@CeO_2 CSNs. The above results further demonstrated the efficient protective effect of CuO_x–CeO_2 nanospheres on the entrapped Au NPs, and thus resulted in the improved resistance to sintering [55].

2.4 Catalytic performance of Au@CuO_x–CeO_2_700 CSNs for p-nitrophenol reduction

The hydrogenation of p-nitrophenol was further utilized in order to better evaluate the effect of high-temperature treatment on the catalytic performance of these as-calcinated catalysts. As observed from Fig. 8(a), Au@CuO_x–CeO_2_700 CSNs can achieve the 100% p-nitrophenol conversion efficiency in less than 10 min, which should be the highest catalytic activity when compared with the Au@CeO_2_700 CSNs (> 45 min, Fig. 8(b)) and CuO_x–CeO_2_700 counterparts (> 60 min, Fig. 8(c)), respectively. Moreover, a linear relationship can be obtained in Fig. 8(d) through fitting the value of $\ln(C_t/C_0)$ and the corresponding reaction time, which conforms to the first-order kinetic reaction. As a result, the resulting apparent rate constant (k) shown in Fig. 8(e) for Au@CuO_x–CeO_2_700 CSNs was calculated to be 1.27 min^{-1}, which maintained 81.4% of the uncalcined Au@CuO_x–CeO_2 CSNs. In contrast, k for Au@CeO_2_700 CSNs and CuO_x–CeO_2_700 dropped sharply to be 0.07 and 0.15 min^{-1}, respectively. As compared with Au@CeO_2_700 CSNs, the introduction of CuO_x to Au@CuO_x–CeO_2_700 CSNs effectively promoted the catalytic activity by 18.1 times. In addition, the catalytic activity of Au@CuO_x–CeO_2_700 CSNs ulteriorly promoted by 8.5 times in comparison to CuO_x–CeO_2_700. Figure 8(f) exhibited the results of recycling catalytic experiments over Au@CuO_x–CeO_2_700 CSNs. Even after five catalytic cycles, no significant activity loss can be observed, while the complete conversion of p-nitrophenol to p-aminophenol over Au@CuO_x–CeO_2_700 CSNs can still be achieved within 10 min, further confirming their excellent durability. Definitely, the above results prove the vital role of CuO_x–CeO_2 in enhancing the sinter resistance of embedded Au NPs. As a result, the unique Au/CuO_x/CeO_2 triphasic interface should benefit to the enhancement of the thermal stability as well as the catalytic performance due to the well-known synergistic catalysis effect [49, 56–58].

2.5 Catalytic mechanism of Au/CuO_x/CeO_2 triphasic interface

To further understand the catalytic mechanism of Au/CuO_x/CeO_2 triphasic interface towards efficient reduction of p-nitrophenol, we conducted density functional theory (DFT) analyses. The most stable molecular configurations of p-nitrophenol on different support surface as well as the binding energies between p-nitrophenol and the support surfaces were firstly optimized. As shown in Fig. 9(a), the optimized structure of p-nitrophenol lying parallel to Au(111) surface, with the adsorption energy of ca. −0.16 eV, which corresponds to the weak physical-adsorption. Moreover, for the CeO_2(111) surface (Fig. 9(b)), the optimal configuration can be described as the hydroxyl group of p-nitrophenol pointing perpendicular to CeO_2(111) surface. The resulting adsorption energy decreased to ca. −0.46 eV, which indicates stronger adsorption strength. However, when Cu_2O_2 clusters are introduced on CeO_2(111) surface, as illustrated in Fig. 9(c), the corresponding adsorption energy of p-nitrophenol can be further reduced to ca. −0.66 eV when the nitro-group of p-nitrophenol directly bind to the Cu atoms, which promoted the nitro-group closer to the surface of nanocatalysts. This result declared that Cu_2O_2 clusters exhibited a stronger interaction with p-nitrophenol as compared to bare Au and CeO_2, and thus facilitated the adsorption of p-nitrophenol molecules [36]. On the one hand, as a general rule, when the reactant molecules have weak interaction with the catalyst, a reaction is hard to occur. As a result, the reference catalysts of Au@CeO_2 CSNs showed the lowest reaction rate

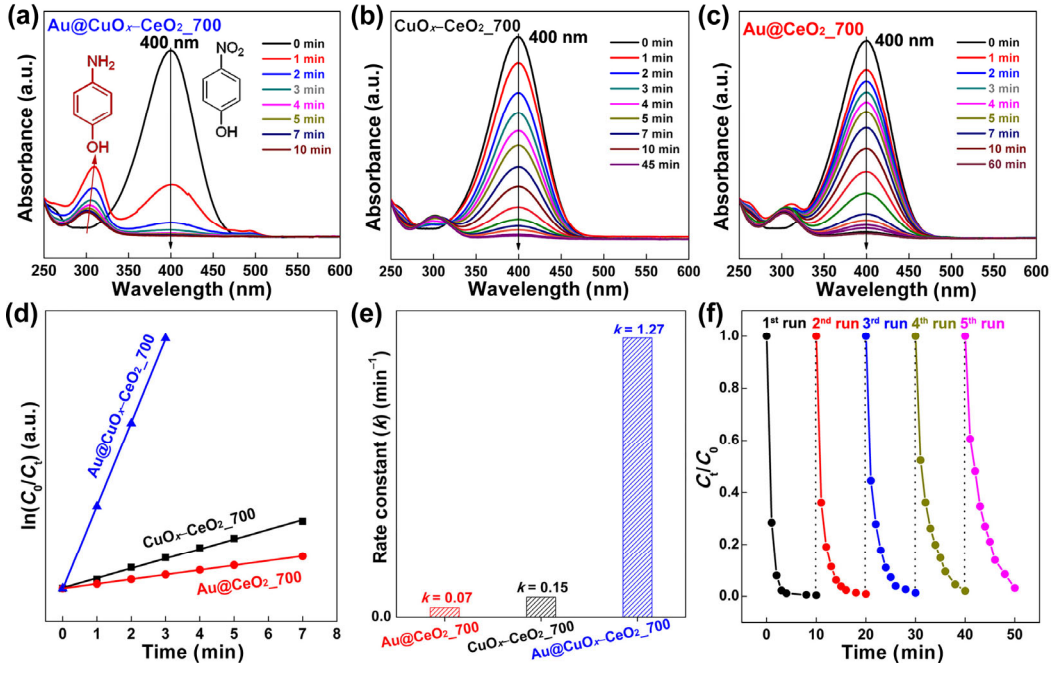

Figure 8 UV–vis absorbance spectra for the catalytic reduction of p-nitrophenol to p-aminophenol over as-prepared catalysts at ambient temperature. (a) Au@CuO_x–CeO_2_700 CSNs, (b) CuO_x–CeO_2_700, and (c) Au@CeO_2_700 CSNs, respectively. (d) Plots of $\ln(C_0/C_t)$ against the reaction time of as-measured catalysts. (e) The corresponding histogram of rate constants. (f) The recycling tests of Au@CuO_x–CeO_2_700 CSNs for the hydrogenation of p-nitrophenol over five cycles.

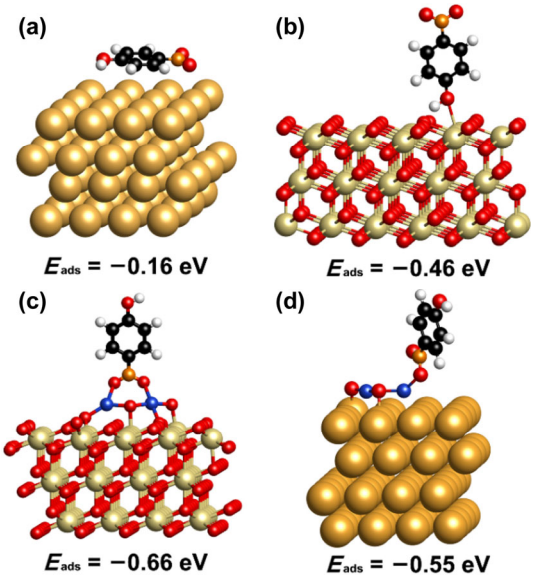

Figure 9 DFT-optimized adsorption configurations and the calculated adsorption energies (E_{ads}) of p-nitrophenol on Au(111) surface (a), CeO_2(111) surface (b), Cu_2O_2–CeO_2(111) surface (c), and Cu_2O_2–CeO_2(111) surface (d).

constant. On the other hand, the strongly-bounded adsorbates will hinder the activation of reactants as well as the desorption of the products. Hence, the CuO_x–CeO_2 counterparts only exhibited the limited catalytic performance due to the overbinding effect. However, as shown in Fig. 9(d), the obtained adsorption energy of p-nitrophenol bound to Au(111)-supported Cu_2O_2 clusters (−0.55 eV) has an increase of 0.11 eV in comparison with Cu_2O_2 clusters on the CeO_2(111) surface. As a result, the combination of Au NPs and CuO_x clusters should be conducive to reach balanced adsorption energy, thus contributing to the strongly enhanced catalytic activity of Au@CuO_x–CeO_2 CSNs [59]. Furthermore, the length of the N–O bond on the Au(111)-supported Cu_2O_2 clusters, CeO_2(111)-supported Cu_2O_2 clusters, CeO_2(111), and Au(111), were calculated to be 1.29, 1.29, 1.25, and 1.25 Å, respectively. The longer N–O bond should be attributed to the electron donation from O atom to the Cu_2O_2 clusters, thus efficiently promoting the cleavage of N–O bonds [36].

In addition to the p-nitrophenol adsorption step, the direct hydrogenation of nitro-group in p-nitrophenol likewise has an essential effect on determining the catalytic activity. Firstly, the vigorous hydrolysis of excessive BH_4^- in aqueous solutions can provide abundant H_2 in a short time, which is evidenced by continuous bubbles spilling from the reaction vessel [60]. Subsequently, with the presence of Au-based catalysts, the as-formed H_2 can dissociate on the catalyst surface to produce metal-H bonds [61], and then reacted with the surrounding p-nitrophenol molecules to give the final product of p-aminophenol. Consequently, we further performed the DFT calculation for the dissociation energy of hydrogen over the as-mentioned nanocatalysts. Considering that CuO_x clusters have strong interaction with adsorbed p-nitrophenol molecules, and this could severely hinder the subsequent dissociation of H–H bonds. Therefore, only Au NPs and CeO_2 NPs have been taken into consideration for the breakage of H–H bonds. According to the calculations, the most favourable dissociation energy of H_2 on the surface of Au(111) is calculated to be 0.19 eV, which is weaker than that (−0.38 eV) on the clean CeO_2(111) surface. Nevertheless, on the one hand, from the resulting DFT-simulated equilibrium phase diagram of steady H*-coverage over the CeO_2(111) surface shown in Fig. S16 in the ESM, the stable H*-coverage on the CeO_2(111) surface was calculated to be about 1/16 monolayer at ambient temperature with the presence of specified amount of hydrogen. On the other hand, supposing that the stable H*-coverage on the CeO_2(111) surface can reach the high coverage of 1/2 monolayer, the corresponding H_2 dissociation energy will significantly increase to ca. 0.26 eV, which should not be favourable for cleaving the H–H bonds. Thus, once the surface of CeO_2(111) have been occupied with trace amounts of H* atoms in a short time, the dissociation of H_2 can also be continuously carried out on the Au NPs surface, which is in accordance with the fact that Au NPs-based materials have been widely-recognized as potential candidate catalysts for hydrogen dissociation [62].

Based on these results, we can put forward a conceivable synergistic catalysis mechanism between Au/CuO_x/CeO_2 triphasic interfaces (Fig. 10). Here, the reactant p-nitrophenol molecules are predominantly adsorbed on CuO_x clusters that situated around Au NPs with appropriate adsorption energy. Meanwhile, Au NPs contribute mainly to dissociate the H–H bonds while the CeO_2 support can play a vital role of transfer station for as-generated H* species. As a result, these highly-active H* species could pass through the CeO_2 surface through H-spillover route or directly participate in the hydrogenation of p-nitrophenol [63]. Ultimately, the existing Au/CuO_x/CeO_2 triphasic interface dramatically enhances the catalytic activity of Au@CuO_x–CeO_2 CSNs towards the reduction of p-nitrophenol through the widely-known synergistic catalysis effect [7, 64, 65]. More significantly, this unique synergy catalysis routine can similarly be achieved by the comparable triphasic system of Pt@CuO_x–CeO_2 CSNs composites (Fig. S17 in the ESM).

3 Conclusions

To summarize, we have developed a convenient method for the one-pot synthesis of Au NPs embedded CuO_x–CeO_2 core/shell composites as highly reactive and sinter-resistant catalysts for catalytic reduction of p-nitrophenol at room temperature. The dual-oxide support of CuO_x–CeO_2, with the ingenious integration of weakly-interacting CuO_x clusters that highly-dispersed on strongly-interacting CeO_2 nanospheres, can play the dual role of both physical barriers and energy barriers, and thus the kinetic mobility as well as the coalescence of embedded Au NPs can be effectively suppressed. Moreover, DFT calculations that attempted to understand the synergistic catalysis by Au@CuO_x–CeO_2 CSNs indicating that CuO_x clusters around the embedded Au NPs is beneficial to achieving the moderate adsorption strength of p-nitrophenol molecules, while the H–H bonds are apt to be synergistically cleaved into H* species on CeO_2-supported Au NPs, and thus react with the p-nitrophenol to directly obtain the last products of p-aminophenol. Therefore, the as-prepared Au@CuO_x–CeO_2 CSNs with novel triphasic core/shell nanostructures showed

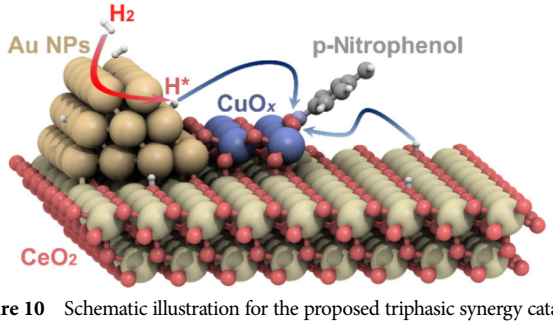

Figure 10 Schematic illustration for the proposed triphasic synergy catalysis mechanism between the Au/CuO_x/CeO_2 interfaces in Au@CuO_x–CeO_2 CSNs.

remarkably enhanced thermal stability against sintering up to 700 °C, and exhibited excellent catalytic performance as well as satisfactory durability towards the reduction of p-nitrophenol before and after high-temperature calcination treatment. This work provides a powerful strategy to prepare new-concept multiphasic nanocatalysts for achieving a marvelous balance between the sinter resistance and catalytic performance. Meaningfully, we prospect this versatile synthetic approach can provide a guideline for rational fabrication of sinter-resistant catalysts towards long-term industrial applications.

4 Experimental

4.1 Materials

$Ce(NO_3)_3·6H_2O$ (A.R., Xilong Chemical Co. Ltd, China), NaOH (G.R., Sinopharm Chemical Reagent Co. Ltd, China), $C_6H_5NO_3$ and $NaBH_4$ (A.R., Sinopharm Chemical Reagent Co. Ltd, China), $HAuCl_4·4H_2O$ (A.R., Beijing Chemical Works, China), K_2PtCl_4 (A.R., Beijing Tongguang Fine Chemicals Corp., China), $CuCl_2·2H_2O$ (A.R., Beijing Hongxing Chemical Factory, China), and ethanol (A.R., Beijing Chemical Works, China) were used as received. Deionized (DI) water (Millipore, 18.2 MΩ·cm) obtained from Milli-Q ultrapure water purification systems was used in all our experiments.

4.2 Preparation of Au@CuO_x–CeO_2 CSNs

In a typical preparation, 1 mmol $Ce(NO_3)_3·6H_2O$ was added to 120 mL deionized water and placed in a 250 mL three-necked flask. After vigorous stirring for 10 min, the mixture was hold under vacuum for 20 min to remove the intrinsic air. Then, 5 mL NaOH aqueous solution (0.4 M) was quickly added into the above solution with subsequent vigorous agitation for 10 min under N_2 atmosphere. After that, 10 mL mixed solution, containing $HAuCl_4$ (0.25 mmol) and $CuCl_2$ (0.75 mmol) was rapidly injected to the as-formed homogeneous solution. The above slurry was maintained at room temperature (25 °C) for 60 min by a temperature controller under N_2 protection. The final products were separated by centrifugation, and washed with water/ethanol for several times. Finally, the obtained powders were dried in a vacuum oven overnight at 40 °C, and annealed at 300 °C in a muffle furnace for 4 h. Analogously, the reference catalysts of Au@CeO_2 core/shell nanospheres (Au/CeO_2 CSNs) were also prepared under identical procedures without the addition of $CuCl_2$. Furthermore, K_2PtCl_4 was used in combination with $CuCl_2$ to produce Pt@CuO_x–CeO_2 CSNs composites. The synthesis process was similar to that of Au@CuO_x–CeO_2 CSNs composites.

4.3 Preparation of CuO_x–CeO_2 reference catalysts

The reference catalysts of CuO_x–CeO_2 nanocomposites (CuO_x–CeO_2) were prepared according to previously reported procedure via a deposition-precipitation approach. Firstly, spherical CeO_2 NPs were synthesized in accordance to reported literature [66]. Then, 200 mg CeO_2 powders were added to 20 mL DI water and stirred intensely for 30 min. Over the subsequent 10 min, 3 mL $CuCl_2$ solution (0.025 M) was added to the above suspension dropwise to obtain ca. 2.4 wt.% Cu loading. During this period, 0.1 M Na_2CO_3 solution was added to maintain the pH at around 9. And then, the mixture solution was kept stirring for 1 h at 25 °C to reach deposition-precipitation equilibrium. The resulting precipitate was collected by centrifugation, washed several times with water and ethanol, and dried at 40 °C overnight. Finally, the obtained products were calcinated at 300 °C in a muffle furnace for 4 h and denoted as CuO_x–CeO_2 nanocomposites.

4.4 Catalytic reduction of p-nitrophenol

The catalytic hydrogenation of p-nitrophenol by excess $NaBH_4$ at room temperature was selected as a probe reaction to explore the catalytic performance of as-prepared catalysts. Typically, 0.3 μmol p-nitrophenol was firstly dissolved into 2 mL DI water in a quartz cuvette. Then, 1 mL freshly-prepared $NaBH_4$ ice-solution (0.25 M) was infused as fast as possible. Subsequently, after mild shaking, 20 μL dispersed catalyst suspension (1 $mg·mL^{-1}$) was quickly injected into the cuvette to give rise to the hydrogenation reaction. The reaction progress was monitored through a UV–vis spectrometer at a regular interval. For a recycling experiment, once the reduction reaction had finished, 0.3 μmol p-nitrophenol were repeatedly added into reaction cuvette for subsequent cycling experiments while the other reaction conditions were fixed. The recyclability experiments were carried out for five successive runs.

4.5 Apparatus

TEM images, HRTEM images, HAADF-STEM images and EDS results were obtained on a JEOL JEM-2100F instrument with accelerating voltage of 200 kV. All TEM samples were prepared by drying a drop of colloidal suspensions on nickel grids coated with carbon film. XRD patterns were measured from a PANalytical X'pert3 powder diffractometer equipped with Cu Kα radiation source (40 kV, 40 mA, λ = 1.5418 Å). XPS data were recorded on an Axi Ultra X-ray imaging photoelectron spectrometer using monochromatised Al Kα radiation to analyze the surface element compositions of the samples. All the binding energies were calibrated according to the reference peak energy of C 1s (284.8 eV). The results of BET surface area were determined via nitrogen adsorption–desorption isotherms (SADI) experiments at 77 K using ASAP 2010 physic-sorption analyzer (Micromeritics). The corresponding pore size distribution and pore volume were calculated on the basis of BJH method. The accurate metal element contents were collected by an ICP-OES (Leeman, Prodigy 7, USA). The hydrodynamic diameter results were obtained through dynamic light scattering (DLS) measurements employing a nanoparticle analyzer (SZ-100, HORIBA).

4.6 XAFS

XAFS analysis of Cu K-edge (E_0 = 8,979 eV) and Au L_3-edge (E_0 = 11,919 eV) were performed at BL14W1 beamline of Shanghai Synchrotron Radiation Facility (SSRF). The electron beam energy was 3.5 GeV, and the stored current was operated at a constant value of 240 mA (top-up mode). The investigated sample powders were ground and pressed as pellets with boron nitrides as diluent. The XAFS data for as-measured nanocatalysts were recorded under fluorescence mode, using a Lytle-type ion chamber and a Si(111) double-crystal monochromator. The resulting XANES results were background-corrected and normalized using the Athena program. For the EXAFS part, the FT of the k^3-weighed data were processed using first-shell approximate and analyzed by employing Artemis codes (k range of 3–12 $Å^{-1}$).

4.7 CO-DRIFTs

In-situ CO diffuse reflectance infrared Fourier transform spectra (CO-DRIFTS) were obtained using a Bruker Tensor-27 Fourier infrared spectrometer equipped with a mercury–cadmium–telluride (MCT) detector. Firstly, 25 mg fresh catalysts were filled into DRIFTS cell (Harrick Scientific Products Inc.) and pre-treated at 573 K with pure He (30 $mL·min^{-1}$) for 30 min to remove residual H_2O and other surficial adsorbates. Then,

the background spectra were collected when the reaction cell cooled to ambient temperature. Afterwards, 5% CO/He (20 mL·min^{-1}) was introduced to the catalysts and maintained for 30 min. Finally, the CO-DRIFTS results were obtained at a resolution of 2 cm^{-1} by averaging 100 scans.

4.8 First-principles computational methods

The density functional calculations were carried out using the Vienna *Ab initio* Simulation Package (VASP) [67–69], with the plane-wave basis of cut-off energy set at 400 eV. The Perdew–Burke–Ernzerhof generalized gradient approximation (GGA-PBE) was employed to describe the exchange–correlation energy functional [70], and the projector augmented wave (PAW) pseudopotentials was utilized to describe the core electrons interaction [71]. All components of free energies were derived with GGA plus Hubbard-U corrections (GGA+U), with the U value of Ce of 4.5 eV, and Cu of 4.0 eV [72].

The fluorite structured CeO_2 and *fcc* phased Au unitcell was used for the (111) surface cleavage. The Cu_2O_2 clusters were supported on the Au(111) and CeO_2(111) surfaces for further computations. For the surface calculations, the top half of layers were relaxed until the residual force was less than 0.05 eV/Å and the vacuum region was set to 15 Å between the slabs. The auto generated k–point sampling of the slab models was set to 2 × 2 × 1.

The adsorption energy (E_{ads}) of p-nitrophenol can be classified as $E_{ads} = E_{M/ads} - E_M - E_{adsorbate}$, in which $E_{M/ads}$ is the total energy of the slab with adsorbates, E_M is the energy of the Au, Cu_2O_2 clusters or CeO_2 slab, and $E_{adsorbate}$ is the energy of the adsorbed molecules in the gas phase. All the energies referred to pre-optimised systems.

Acknowledgements

The authors are grateful for the financial support of the National Natural Science Foundation of China (Nos. 21590791, 21771005, 21931001, and 21927901), and Ministry of Science and Technology (MOST) of China (Nos. 2014CB643803, 2017YFA0205101, and 2017YFA0205104). The computational work was supported by the High–performance Computing Platform of Peking University. K. W. specifically thanks the National Postdoctoral Program for Innovative Talents under grant No. BX20190005, and the China Postdoctoral Science Foundation (No. 2019M660293).

Electronic Supplementary Material: Supplementary material (more composition characterizations from ICP-OES and XPS results, TEM images of Pt@CuO_x–CeO_2 CSNs, Au@CeO_2 CSNs, CuO_x–CeO_2 reference catalysts and spent Au@CuO_x–CeO_2 CSNs composite catalysts, hydrodynamic diameter distribution, EXAFS fitting results, and CO-DRIFTs profiles of Au@CuO_x–CeO_2 CSNs, XPS survey spectrum of Au@CeO_2 CSNs, N_2 adsorption–desorption isotherms, TEM images, and XRD patterns of Au@CeO_2_700 CSNs and CuO_x–CeO_2_700, a comparison table of rate constants (k) of p-nitrophenol reduction reaction, DFT-simulated equilibrium phase diagrams and p-nitrophenol catalytic reduction performance of Pt@CuO_x–CeO_2 CSNs) is available in the online version of this article at https://doi.org/10.1007/s12274-020-2806-9.

References

[1] Zhang, J. M.; Chen, G. Z.; Chaker, M.; Rosei, F.; Ma, D. L. Gold nanoparticle decorated ceria nanotubes with significantly high catalytic activity for the reduction of nitrophenol and mechanism study. *Appl. Catal. B: Environ.* **2013**, *132–133*, 107–115.

[2] Rogers, S. M.; Catlow, C. R. A.; Gianolio, D.; Wells, P. P.; Dimitratos, N. Supported metal nanoparticles with tailored catalytic properties through sol-immobilisation: Applications for the hydrogenation of nitrophenols. *Faraday Discuss.* **2018**, *208*, 443–454.

[3] Wu, Y. H.; Li, C. Y.; Zhou, K. W.; Zhao, Y. H.; Wang, X. J. A new preparation strategy via an *in situ* catalytic process: CeO_2@Ag/$Ag_2Ta_4O_{11}$ catalyst for 4-nitrophenol reduction. *CrystEngComm* **2016**, *18*, 6513–6519.

[4] Qi, J.; Chen, J.; Li, G. D.; Li, S. X.; Gao, Y.; Tang, Z. Y. Facile synthesis of core–shell Au@CeO_2 nanocomposites with remarkably enhanced catalytic activity for CO oxidation. *Energy Environ. Sci.* **2012**, *5*, 8937–8941.

[5] Corma, A.; Garcia, H. Supported gold nanoparticles as catalysts for organic reactions. *Chem. Soc. Rev.* **2008**, *37*, 2096–2126.

[6] Dai, Y. Q.; Lu, P.; Cao, Z. M.; Campbell, C. T.; Xia, Y. N. The physical chemistry and materials science behind sinter-resistant catalysts. *Chem. Soc. Rev.* **2018**, *47*, 4314–4331.

[7] Bingwa, N.; Patala, R.; Noh, J. H.; Ndolomingo, M. J.; Tetyana, S.; Bewana, S.; Meijboom, R. Synergistic effects of gold–palladium nanoalloys and reducible supports on the catalytic reduction of 4-nitrophenol. *Langmuir* **2017**, *33*, 7086–7095.

[8] Xu, P. F.; Yu, R. B.; Ren, H.; Zong, L. B.; Chen, J.; Xing, X. R. Hierarchical nanoscale multi-shell Au/CeO_2 hollow spheres. *Chem. Sci.* **2014**, *5*, 4221–4226.

[9] Ta, N.; Liu, J. Y.; Chenna, S.; Crozier, P. A.; Li, Y.; Chen, A. L.; Shen, W. J. Stabilized gold nanoparticles on ceria nanorods by strong interfacial anchoring. *J. Am. Chem. Soc.* **2012**, *134*, 20585–20588.

[10] Wu, K.; Sun, L. D.; Yan, C. H. Recent progress in well-controlled synthesis of ceria-based nanocatalysts towards enhanced catalytic performance. *Adv. Energy Mater.* **2016**, *6*, 1600501.

[11] Vivier, L.; Duprez, D. Ceria-based solid catalysts for organic chemistry. *ChemSusChem* **2010**, *3*, 654–678.

[12] Guo, L. W.; Du, P. P.; Fu, X. P.; Ma, C.; Zeng, J.; Si, R.; Huang, Y. Y.; Jia, C. J.; Zhang, Y. W.; Yan, C. H. Contributions of distinct gold species to catalytic reactivity for carbon monoxide oxidation. *Nat. Commun.* **2016**, *7*, 13481.

[13] Zhou, H. P.; Wu, H. S.; Shen, J.; Yin, A. X.; Sun, L. D.; Yan, C. H. Thermally stable Pt/CeO_2 hetero-nanocomposites with high catalytic activity. *J. Am. Chem. Soc.* **2010**, *132*, 4998–4999.

[14] Jia, H. L.; Zhu, X. M.; Jiang, R. B.; Wang, J. F. Aerosol-sprayed gold/ceria photocatalyst with superior plasmonic hot electron-enabled visible-light activity. *ACS Appl. Mater. Interfaces* **2017**, *9*, 2560–2571.

[15] Jia, H. L.; Du, A. X.; Zhang, H.; Yang, J. H.; Jiang, R. B.; Wang, J. F.; Zhang, C. Y. Site-selective growth of crystalline ceria with oxygen vacancies on gold nanocrystals for near-infrared nitrogen photofixation. *J. Am. Chem. Soc.* **2019**, *141*, 5083–5086.

[16] Li, J.; Song, S. Y.; Long, Y.; Wu, L. L.; Wang, X.; Xing, Y.; Jin, R. C.; Liu, X. G.; Zhang, H. J. Investigating the hybrid-structure-effect of CeO_2-encapsulated Au nanostructures on the transfer coupling of nitrobenzene. *Adv. Mater.* **2018**, *30*, 1704416.

[17] Li, J.; Song, S. Y.; Long, Y.; Yao, S.; Ge, X.; Wu, L. L.; Zhang, Y. B.; Wang, X.; Yang, X. G.; Zhang, H. J. A general one-pot strategy for the synthesis of Au@multi-oxide yolk@shell nanospheres with enhanced catalytic performance. *Chem. Sci.* **2018**, *9*, 7569–7574.

[18] Li, B. X.; Gu, T.; Ming, T.; Wang, J. X.; Wang, P.; Wang, J. F.; Yu, J. C. (Gold core)@(ceria shell) nanostructures for plasmon-enhanced catalytic reactions under visible light. *ACS Nano* **2014**, *8*, 8152–8162.

[19] Min, B. K.; Wallace, W. T.; Goodman, D. W. Synthesis of a sinter-resistant, mixed-oxide support for Au nanoclusters. *J. Phys. Chem. B* **2004**, *108*, 14609–14615.

[20] Lu, P.; Campbell, C. T.; Xia, Y. N. A sinter-resistant catalytic system fabricated by maneuvering the selectivity of SiO_2 deposition onto the TiO_2 surface versus the Pt nanoparticle surface. *Nano Lett.* **2013**, *13*, 4957–4962.

[21] Bauer, J. C.; Veith, G. M.; Allard, L. F.; Oyola, Y.; Overbury, S. H.; Dai, S. Silica-supported Au–CuO_x hybrid nanocrystals as active and selective catalysts for the formation of acetaldehyde from the oxidation of ethanol. *ACS Catal.* **2012**, *2*, 2537–2546.

[22] Wang, F.; Li, W.; Feng, X. L.; Liu, D. P.; Zhang, Y. Decoration of Pt on Cu/Co double-doped CeO_2 nanospheres and their greatly enhanced catalytic activity. *Chem. Sci.* **2016**, *7*, 1867–1873.

[23] Prucek, R.; Kvítek, L.; Panáček, A.; Vančurová, L.; Soukupová, J.; Jančík, D.; Zbořil, R. Polyacrylate-assisted synthesis of stable copper nanoparticles and copper(I) oxide nanocubes with high catalytic efficiency. *J. Mater. Chem.* **2009**, *19*, 8463–8469.

[24] Dai, Y. Q.; Lim, B.; Yang, Y.; Cobley, C. M.; Li, W. Y.; Cho, E. C.; Grayson, B.; Fanson, P. T.; Campbell, C. T.; Sun, Y. M. et al. A sinter-resistant catalytic system based on platinum nanoparticles supported on TiO_2 nanofibers and covered by porous silica. *Angew. Chem., Int. Ed.* **2010**, *49*, 8165–8168.

[25] Song, S. Y.; Wang, X.; Zhang, H. J. CeO_2-encapsulated noble metal nanocatalysts: Enhanced activity and stability for catalytic application. *NPG Asia Mater.* **2015**, *7*, e179.

[26] Wu, K.; Fu, X. P.; Yu, W. Z.; Wang, W. W.; Jia, C. J.; Du, P. P.; Si, R.; Wang, Y. H.; Li, L. D.; Zhou, L. et al. Pt-embedded CuO_x–CeO_2 multicore–shell composites: Interfacial redox reaction-directed synthesis and composition-dependent performance for CO oxidation. *ACS Appl. Mater. Interfaces* **2018**, *10*, 34172–34183.

[27] Wang, X.; Liu, D. P.; Song, S. Y.; Zhang, H. J. Pt@CeO_2 Multicore@Shell self-assembled nanospheres: Clean synthesis, structure optimization, and catalytic applications. *J. Am. Chem. Soc.* **2013**, *135*, 15864–15872.

[28] Wang, W. W.; Yu, W. Z.; Du, P. P.; Xu, H.; Jin, Z.; Si, R.; Ma, C.; Shi, S.; Jia, C. J.; Yan, C. H. Crystal plane effect of ceria on supported copper oxide cluster catalyst for CO oxidation: Importance of metal–support interaction. *ACS Catal.* **2017**, *7*, 1313–1329.

[29] Xia, Y. S.; Nguyen, T. D.; Yang, M.; Lee, B.; Santos, A.; Podsiadlo, P.; Tang, Z. Y.; Glotzer, S. C.; Kotov, N. A. Self-assembly of self-limiting monodisperse supraparticles from polydisperse nanoparticles. *Nat. Nanotechnol.* **2011**, *6*, 580–587.

[30] Khan, M. M.; Ansari, S. A.; Ansari, M. O.; Min, B. K.; Lee, J.; Cho, M. H. Biogenic fabrication of Au@CeO_2 nanocomposite with enhanced visible light activity. *J. Phys. Chem. C* **2014**, *118*, 9477–9484.

[31] Hu, Z.; Liu, X. F.; Meng, D. M.; Guo, Y.; Guo, Y. L.; Lu, G. Z. Effect of ceria crystal plane on the physicochemical and catalytic properties of Pd/Ceria for CO and propane oxidation. *ACS Catal.* **2016**, *6*, 2265–2279.

[32] Mitsudome, T.; Yamamoto, M.; Maeno, Z.; Mizugaki, T.; Jitsukawa, K.; Kaneda, K. One-step synthesis of core-gold/shell-ceria nanomaterial and its catalysis for highly selective semihydrogenation of alkynes. *J. Am. Chem. Soc.* **2015**, *137*, 13452–13455.

[33] Zhao, P. X.; Feng, X. W.; Huang, D. S.; Yang, G. Y.; Astruc, D. Basic concepts and recent advances in nitrophenol reduction by gold- and other transition metal nanoparticles. *Coord. Chem. Rev.* **2015**, *287*, 114–136.

[34] Aditya, T.; Pal, A.; Pal, T. Nitroarene reduction: A trusted model reaction to test nanoparticle catalysts. *Chem. Commun.* **2015**, *51*, 9410–9431.

[35] Cheng, X. S.; Wang, D. X.; Liu, J. C.; Kang, X.; Yan, H. J.; Wu, A. P.; Gu, Y.; Tian, C. G.; Fu, H. G. Ultra-small Mo_2N on SBA-15 as a highly efficient promoter of low-loading Pd for catalytic hydrogenation. *Nanoscale* **2018**, *10*, 22348–22356.

[36] Cai, R. S.; Ellis, P. R.; Yin, J. L.; Liu, J.; Brown, C. M.; Griffin, R.; Chang, G. J.; Yang, D. J.; Ren, J.; Cooke, K. et al. Performance of preformed Au/Cu Nanoclusters deposited on MgO powders in the catalytic reduction of 4-nitrophenol in solution. *Small* **2018**, *14*, 1703734.

[37] Evangelista, V.; Acosta, B.; Miridonov, S.; Smolentseva, E.; Fuentes, S.; Simakov, A. Highly active Au-CeO_2@ZrO_2 yolk–shell nanoreactors for the reduction of 4-nitrophenol to 4-aminophenol. *Appl. Catal. B: Environ.* **2015**, *166–167*, 518–528.

[38] Zheng, J. M.; Dong, Y. L.; Wang, W. F.; Ma, Y. H.; Hu, J.; Chen, X. J.; Chen, X. G. *In situ* loading of gold nanoparticles on Fe_3O_4@SiO_2 magnetic nanocomposites and their high catalytic activity. *Nanoscale* **2013**, *5*, 4894–4901.

[39] Gao, G.; Xi, Q. Y.; Zhang, Y. Q.; Jin, M. Y.; Zhao, Y. X.; Wu, C. Q.; Zhou, H.; Guo, P. R.; Xu, J. W. Atomic-scale engineering of MOF array confined Au nanoclusters for enhanced heterogeneous catalysis. *Nanoscale* **2019**, *11*, 1169–1176.

[40] Zhang, C.; Cheng, X.; Guo, Z. M.; Lv, Z. G. A multi-metal PtAgAu@CeO_2 core–shell nanocatalyst with improved catalytic performance. *New J. Chem.* **2019**, *43*, 561–563.

[41] Li, K. K.; Jiao, T. F.; Xing, R. R.; Zou, G. D.; Zhou, J. X.; Zhang, L. X.; Peng, Q. M. Fabrication of tunable hierarchical MXene@AuNPs nanocomposites constructed by self-reduction reactions with enhanced catalytic performances. *Sci. China Mater.* **2018**, *61*, 728–736.

[42] Lv, J. J.; Wang, A. J.; Ma, X. H.; Xiang, R. Y.; Chen, J. R.; Feng, J. J. One-pot synthesis of porous Pt–Au nanodendrites supported on reduced graphene oxide nanosheets toward catalytic reduction of 4-nitrophenol. *J. Mater. Chem. A* **2015**, *3*, 290–296.

[43] Lee, S.; Seo, J.; Jung, W. C. Sintering-resistant Pt@CeO_2 nanoparticles for high-temperature oxidation catalysis. *Nanoscale* **2016**, *8*, 10219–10228.

[44] Yang, C. W.; Yu, X. J.; Heißler, S.; Nefedov, A.; Colussi, S.; Llorca, J.; Trovarelli, A.; Wang, Y. M.; Wöll, C. Surface faceting and reconstruction of ceria nanoparticles. *Angew. Chem., Int. Ed.* **2017**, *56*, 375–379.

[45] Chen, G. Z.; Guo, Z. Y.; Zhao, W.; Gao, D. W.; Li, C. C.; Ye, C.; Sun, G. X. Design of porous/hollow structured ceria by partial thermal decomposition of Ce-MOF and selective etching. *ACS Appl. Mater. Interfaces* **2017**, *9*, 39594–39601.

[46] Wang, W. W.; Du, P. P.; Zou, S. H.; He, H. Y.; Wang, R. X.; Jin, Z.; Shi, S.; Huang, Y. Y.; Si, R.; Song, Q. S. et al. Highly dispersed copper oxide clusters as active species in copper-ceria catalyst for preferential oxidation of carbon monoxide. *ACS Catal.* **2015**, *5*, 2088–2099.

[47] Li, W. Z.; Kovarik, L.; Mei, D. H.; Liu, J.; Wang, Y.; Peden, C. H. F. Stable platinum nanoparticles on specific $MgAl_2O_4$ spinel facets at high temperatures in oxidizing atmospheres. *Nat. Commun.* **2013**, *4*, 2481.

[48] Liu, X. Y.; Wang, A. Q.; Li, L.; Zhang, T.; Mou, C. Y.; Lee, J. F. Structural changes of Au–Cu bimetallic catalysts in CO oxidation: *In situ* XRD, EPR, XANES, and FT-IR characterizations. *J. Catal.* **2011**, *278*, 288–296.

[49] Wang, Q.; Li, Y. J.; Liu, B. C.; Dong, Q.; Xu, G. R.; Zhang, L.; Zhang, J. Novel recyclable dual-heterostructured Fe_3O_4@CeO_2/M (M = Pt, Pd and Pt–Pd) catalysts: Synergetic and redox effects for superior catalytic performance. *J. Mater. Chem. A* **2015**, *3*, 139–147.

[50] Chen, C.; Fang, X. L.; Wu, B. H.; Huang, L. J.; Zheng, N. F. A multi-yolk–shell structured nanocatalyst containing sub-10 nm Pd nanoparticles in porous CeO_2. *ChemCatChem* **2012**, *4*, 1578–1586.

[51] Guo, X. D.; Kan, H. P.; Liu, X. X.; Geng, H. S.; Wang, L. Y. Facile synthesis of hollow hierarchical Ni@C nanocomposites with well-dispersed high-loading Ni nanoparticles embedded in carbon for reduction of 4-nitrophenol. *RSC Adv.* **2018**, *8*, 15999–16003.

[52] Shao, B.; Zhang, J. Y.; Huang, J. H.; Qiao, B. T.; Su, Y.; Miao, S.; Zhou, Y.; Li, D.; Huang, W. X.; Shen, W. J. Size-dependency of gold nanoparticles on TiO_2 for CO oxidation. *Small* **2018**, *2*, 1800273.

[53] Li, W. G.; Hu, Y. J.; Jiang, H.; Jiang, N.; Bi, W.; Li, C. Z. Litchi-peel-like hierarchical hollow copper-ceria microspheres: Aerosol-assisted synthesis and high activity and stability for catalytic CO oxidation. *Nanoscale* **2018**, *10*, 22775–22786.

[54] Kundu, A.; Park, B.; Ray, C.; Oh, J.; Jun, S. C. Environmentally benign and cost-effective synthesis of water soluble red light emissive gold nanoclusters: Selective and ultra-sensitive detection of mercuric ions. *New J. Chem.* **2019**, *43*, 900–906.

[55] Ye, L.; Duan, X. P.; Wu, S.; Wu, T. S.; Zhao, Y. X.; Robertson, A. W.; Chou, H. L.; Zheng, J. W.; Ayvalı, T.; Day, S. et al. Self-regeneration of Au/CeO_2 based catalysts with enhanced activity and ultra-stability for acetylene hydrochlorination. *Nat. Commun.* **2019**, *10*, 914.

[56] Cai, J. M.; Zhang, J.; Cao, K.; Gong, M.; Lang, Y.; Liu, X.; Chu, S. Q.; Shan, B.; Chen, R. Selective passivation of Pt nanoparticles with enhanced sintering resistance and activity toward CO oxidation via atomic layer deposition. *ACS Appl. Nano Mater.* **2018**, *1*, 522–530.

[57] Liu, B. C.; Wang, Q.; Yu, S. L.; Zhao, T.; Han, J. X.; Jing, P.; Hu, W. T.; Liu, L. X.; Zhang, J.; Sun, L. D. et al. Double shelled hollow nanospheres with dual noble metal nanoparticle encapsulation for enhanced catalytic application. *Nanoscale* **2013**, *5*, 9747–9757.

[58] Chen, G. Z.; Wang, Y.; Wei, Y. W.; Zhao, W.; Gao, D. W.; Yang, H. X.; Li, C. C. Successive interfacial reaction-directed synthesis of CeO_2@Au@CeO_2-MnO_2 environmental catalyst with sandwich hollow structure. *ACS Appl. Mater. Interfaces* **2018**, *10*, 11595–11603.

[59] Pozun, Z. D.; Rodenbusch, S. E.; Keller, E.; Tran, K.; Tang, W. J.; Stevenson, K. J.; Henkelman, G. A systematic investigation of

p-Nitrophenol reduction by bimetallic dendrimer encapsulated nanoparticles. *J. Phys. Chem. C* **2013**, *117*, 7598–7604.

[60] Dai, H. B.; Liang, Y.; Ma, L. P.; Wang, P. New insights into catalytic hydrolysis kinetics of sodium borohydride from Michaelis−Menten model. *J. Phys. Chem. C* **2008**, *112*, 15886–15892.

[61] Wunder, S.; Polzer, F.; Lu, Y.; Mei, Y.; Ballauff, M. Kinetic analysis of catalytic reduction of 4-nitrophenol by metallic nanoparticles immobilized in spherical polyelectrolyte brushes. *J. Phys. Chem. C* **2010**, *114*, 8814–8820.

[62] Mukherjee, S.; Libisch, F.; Large, N.; Neumann, O.; Brown, L. V.; Cheng, J.; Lassiter, J. B.; Carter, E. A.; Nordlander, P.; Halas, N. J. Hot electrons do the impossible: Plasmon-induced dissociation of H_2 on Au. *Nano Lett.* **2013**, *13*, 240–247.

[63] Guo, Y.; Mei, S.; Yuan, K.; Wang, D. J.; Liu, H. C.; Yan, C. H.; Zhang, Y. W. Low-temperature CO_2 methanation over CeO_2-supported Ru single atoms, nanoclusters, and nanoparticles competitively tuned by strong metal–support interactions and H-spillover effect. *ACS Catal.* **2018**, *8*, 6203–6215.

[64] Jiang, H. L.; Xu, Q. Recent progress in synergistic catalysis over heterometallic nanoparticles. *J. Mater. Chem.* **2011**, *21*, 13705–13725.

[65] Duan, X. M.; Liu, J.; Hao, J. F.; Wu, L. M.; He, B. J.; Qiu, Y.; Zhang, J.; He, Z. L.; Xi, J. B.; Wang, S. Magnetically recyclable nanocatalyst with synergetic catalytic effect and its application for 4-nitrophenol reduction and Suzuki coupling reactions. *Carbon* **2018**, *130*, 806–813.

[66] Liang, X.; Xiao, J. J.; Chen, B. H.; Li, Y. D. Catalytically stable and active CeO_2 mesoporous spheres. *Inorg. Chem.* **2010**, *49*, 8188–8190.

[67] Kresse, G.; Hafner, J. *Ab initio* molecular dynamics for open-shell transition metals. *Phys. Rev. B* **1993**, *48*, 13115–13118.

[68] Kresse, G.; Furthmüller, J. Efficient iterative schemes for *ab initio* total-energy calculations using a plane-wave basis set. *Phys. Rev. B* **1996**, *54*, 11169–11186.

[69] Kresse, G.; Furthmüller, J. Efficiency of *ab-initio* total energy calculations for metals and semiconductors using a plane-wave basis set. *Comp. Mater. Sci.* **1996**, *6*, 15–50.

[70] Perdew, J. P.; Burke, K.; Ernzerhof, M. Generalized gradient approximation made simple. *Phys. Rev. Lett.* **1996**, *77*, 3865–3868.

[71] Blöchl, P. E. Projector augmented-wave method. *Phys. Rev. B* **1994**, *50*, 17953–17979.

[72] Ke, J.; Zhu, W.; Jiang, Y. Y.; Si, R.; Wang, Y. J.; Li, S. C.; Jin, C. H.; Liu, H. C.; Song, W. G.; Yan, C. H. et al. Strong local coordination structure effects on subnanometer PtO_x clusters over CeO_2 nanowires probed by low-temperature CO oxidation. *ACS Catal.* **2015**, *5*, 5164–5173.